

# Chapter 14

## Hybrid Mechanical Systems

**Philipp Treutlein, Claudiu Genes, Klemens Hammerer,  
Martino Poggio and Peter Rabl**

**Abstract** We discuss hybrid systems in which a mechanical oscillator is coupled to another (microscopic) quantum system, such as trapped atoms or ions, solid-state spin qubits, or superconducting devices. We summarize and compare different coupling schemes and describe first experimental implementations. Hybrid mechanical systems enable new approaches to quantum control of mechanical objects, precision sensing, and quantum information processing.

### 14.1 Introduction

The ability of functionalized mechanical systems to respond to electric, magnetic and optical forces has in the past led to widespread applications of mechanical resonators as sensitive force detectors. With improved technology the same principle will apply for resonators in the quantum regime and allow the integration of mechanical

---

P. Treutlein (✉) · M. Poggio  
Department of Physics, University of Basel, Basel, Switzerland  
e-mail: philipp.treutlein@unibas.ch

M. Poggio  
e-mail: martino.poggio@unibas.ch

C. Genes  
Institute for Theoretical Physics, University of Innsbruck, Innsbruck, Austria  
e-mail: Claudiu.Genes@uibk.ac.at

K. Hammerer  
Institute for Theoretical Physics and Institute for Gravitational Physics,  
University of Hannover, Hannover, Germany  
e-mail: Klemens.Hammerer@itp.uni-hannover.de

P. Rabl  
Institute of Atomic and Subatomic Physics, Vienna University of Technology,  
Vienna, Austria  
e-mail: peter.rabl@ati.ac.at

oscillators with a large variety of other (microscopic) quantum systems such as atoms and ions, electronic spins, or quantized charge degrees of freedom. The benefits of such hybrid quantum systems are quite diverse. On the one hand, the motion of the resonator can be used as a sensitive probe and readout device for static and dynamic properties of the quantum system. On the other hand, coupling the resonator to a coherent and fully controllable two-level system provides a way to prepare and detect non-classical states of mechanical motion. Finally, the mechanical system can serve as a quantum transducer to mediate interactions between physically quite distinct quantum systems. This can be used to coherently couple e.g. an electronic spin to charge or optical degrees of freedom with various potential applications in the context of (hybrid) quantum information processing.

From a practical point of view the combination of mechanical resonators with microscopic quantum systems faces considerable challenges. Often the functionalization of mechanical resonators with electrodes, magnets, or mirrors competes with the requirement of a small mass to achieve a sufficient coupling strength on a single-quantum level. At the same time both the resonator and the other quantum system must be exceptionally well isolated from the environment to avoid decoherence. Various hybrid setups have been proposed that address those challenges, and some have already been implemented in experiments. This includes solid-state systems such as spin qubits, quantum dots, and superconducting devices, as well as atomic systems such as trapped atoms, ions, and molecules. In this chapter we give a brief overview of the different approaches towards mechanical hybrid quantum systems and discuss some basic examples from the fields of solid-state and atomic physics.

## 14.2 Solid-State Quantum Systems Coupled to Mechanics

Within the field of solid-state physics, a large variety of microscopic two- or few-level systems have been identified that are well isolated from the environment and allow for a coherent manipulation of their quantum state. Examples range from electronic or nuclear spin states associated with naturally occurring defect centers [1] to electronic states of so-called artificial atoms such as quantum dots [2] or superconducting Josephson devices [3]. Nanomechanical systems are naturally integrated with such solid-state quantum systems by fabricating them on the same chip, where they may interact with spins or charges via strong magnetic or electric forces. In contrast to most of the atomic implementations described below, the system dimensions are usually not limited by optical properties or trapping requirements, and without those restrictions strong interactions between an individual two-level system and a mechanical mode can be achieved more easily. On the other hand, it is more challenging to achieve long coherence times in the solid state. In combination with cryogenic temperatures the solid-state approach to mechanical hybrid systems offers a promising route towards manipulating mechanical motion on a single-phonon level.

We first present a brief overview of different physical mechanisms that have been suggested for achieving strong coupling between solid-state systems and mechanical

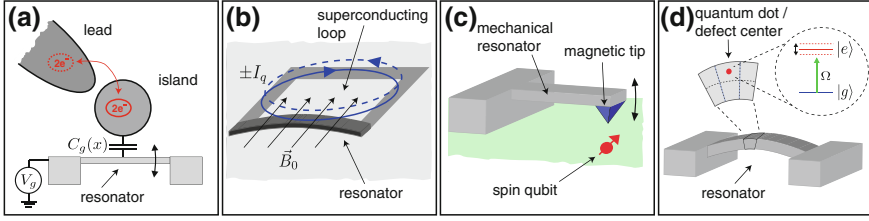


**Fig. 14.1** Different schemes for coupling solid-state qubits and mechanical resonators. **a** Electrostatic coupling to charge qubits. **b** Lorentz force interactions with current states of a flux qubit. **c** Magnetic coupling to spins. **d** Deformation potential coupling to quantum dots or defect centers

motion. For the specific examples of superconducting charge qubits and electronic spin qubits we then describe mechanical sensing techniques and quantum control schemes as basic applications of these systems in the weak and strong interaction regime.

### 14.2.1 Overview of Systems and Coupling Mechanisms

The coupling of mechanical motion to other harmonic oscillators has been treated in other chapters of this book and we restrict the discussion in this section to microscopic two-level systems with a ground and excited state  $|g\rangle$  and  $|e\rangle$ . In solid-state systems the energy separation  $E_{eg}$  between the two states is strongly dependent on the local electrostatic and magnetic fields, which also provides a way to couple to mechanical motion. For example, by fabricating an oscillating electrode or a vibrating magnetic tip, the system energy  $E_{eg}(\hat{x}) = E_{eg}^0 + \partial_x E_{eg} \hat{x} + (1/2) \partial_x^2 E_{eg} \hat{x}^2 + \dots$  now explicitly depends on the resonator displacement  $\hat{x} = x_{\text{ZPF}}(\hat{b} + \hat{b}^\dagger)$ . Even for nanoscale devices the zero point motion  $x_{\text{ZPF}} \approx 10^{-13}$  m is still much smaller than other system dimensions and corrections beyond the linear coupling term are usually negligible. Therefore, the generic Hamiltonian for the qubit-resonator system is given by

$$\hat{H}(t) = \hat{H}_q(t) + \hbar \Omega_M \hat{b}^\dagger \hat{b} + \hbar \lambda (\hat{b} + \hat{b}^\dagger) \hat{\sigma}_z, \quad (14.1)$$

where  $\hat{\sigma}_z = |e\rangle\langle e| - |g\rangle\langle g|$  is the Pauli operator and  $\hat{H}_q(t)$  denotes the unperturbed Hamiltonian for the solid-state qubit. The relevant parameter in Eq. (14.1) is the coupling strength  $\lambda = \partial_x E_{eg} x_{\text{ZPF}} / 2\hbar$ , which is the frequency shift per vibrational quantum.

While the basic form of the interaction in Eq. (14.1) has been derived from quite general considerations, the origin and the magnitude of the qubit-resonator coupling  $\lambda$  depends on the specific physical implementation. Figure 14.1 illustrates four basic mechanisms for coupling different charge and spin qubits to mechanical motion. In Fig. 14.1a two states encoded in quantized charge degrees of freedom, e.g. an electron on a quantum dot [4–7] or a Cooper pair on a small superconducting

island [8–11], are coupled to a vibrating gate electrode. The energy for a total charge  $Q$  on the island is  $E_Q = (Q - Q_g)^2/2C_\Sigma$  where  $C_\Sigma = C_0 + C_g$  is the total capacitance of the island,  $C_g$  the gate capacitance and  $Q_g = V_g C_g$  the gate charge. For small displacements  $C_g(x) \approx C_g(1 - x/d)$  where  $d$  is the gate separation, the typical coupling strength is

$$\hbar\lambda_{el} \approx eV_g C_g / C_\Sigma \times x_{ZPF} / d. \quad (14.2)$$

For  $d \approx 100$  nm and voltages up to  $V_g = 10$  V this coupling is quite substantial and can reach values in the range of  $\lambda_{el}/2\pi \approx 5 - 50$  MHz [8].

Instead of using charge states, a two-level system can alternatively be encoded in clockwise and anti-clockwise circulating currents in a superconducting loop [12–17] as shown in Fig. 14.1b. Here an interaction with a freely suspended arm of the loop can arise from the Lorentz force created by a magnetic field  $B_0$  perpendicular to the bending motion [14–16]. For circulating currents of magnitude  $I_q$  and a length  $l$  of the resonator we obtain

$$\hbar\lambda_{Lor} \approx B_0 I_q l x_{ZPF}. \quad (14.3)$$

Although the applied magnetic field is limited by the critical field of the superconductor,  $B_0 \leq 10$  mT, typical values of  $I_q \approx 100$  nA and  $l = 5$   $\mu$ m still result in a coupling strength of  $\lambda_{Lor}/2\pi \approx 0.1 - 1$  MHz [14–16].

Qubits encoded in electronic or nuclear spin states can be coupled to the motion of a magnetized tip [18–22] as shown in Fig. 14.1c. Here strong magnetic field gradients  $\nabla B$  lead to a position dependent Zeeman splitting of the spin states and for an electron spin,

$$\hbar\lambda_{mag} \approx g_s \mu_B x_{ZPF} \nabla B / 2, \quad (14.4)$$

where  $\mu_B$  is the Bohr magneton and  $g_s \approx 2$ . On the scale of a few nanometers, magnetic field gradients can be as high as  $\nabla B \sim 10^7$  T/m [23, 24], which corresponds to a coupling strength of  $\lambda_{mag}/2\pi \approx 10 - 100$  kHz [22]. Due to a smaller magnetic moment, the coupling to a single nuclear spin is reduced by a factor  $\sim 10^{-3}$ , but is partially compensated by the much longer coherence times of nuclear spin qubits.

Mechanical resonators cannot only modulate the configuration of externally applied fields, but for example also couple to quantum dots or defect centers by changing the local lattice configuration of the host material [25]. This deformation potential coupling is illustrated in Fig. 14.1d where flexural vibrations of the resonator induce a local stress  $\sigma \sim z_0 x_{ZPF} / l^2$ , where  $l$  is the resonator length and  $z_0$  the distance of the defect from the middle of the beam. The corresponding level shift is given by

$$\hbar\lambda_{def} \approx (D_e - D_g) z_0 x_{ZPF} / l^2, \quad (14.5)$$

where  $D_e$  and  $D_g$  are deformation potential constants for the ground and excited electronic states. For quantum dots a coupling strength of  $\lambda_{def}/2\pi \approx 1 - 10$  MHz can be achieved [25], but competes with radiative decay processes of the same order.

In summary, this brief overview shows that various different mechanisms lead to interactions between solid-state two-level systems and mechanical resonators. In many cases the single-phonon coupling strength  $\lambda$  can be comparable to or even exceed the typical decoherence rate of the qubit  $T_2^{-1}$  as well as the mechanical heating rate  $\Gamma_{\text{th}} = k_B T / \hbar Q$ . As we describe now in more detail this enables various applications ranging from measurement and ground state cooling schemes for weak coupling to quantum control techniques in the strong coupling regime.

### 14.2.2 Superconducting Devices and Mechanics

Solid-state qubits which are encoded in a quantized charge degree of freedom can be coupled to mechanical motion via electrostatic interactions. A prototype example is the Cooper Pair Box (CPB), i.e. a small superconducting island where Cooper pairs are coherently coupled to a large reservoir via a Josephson tunnel junction (see Fig. 14.1a). The CPB belongs to a larger class of superconducting qubits [3, 26] and is—in its simplest realization—described by the number  $N$  of excess Cooper pairs on the island and its conjugate variable  $\delta$  which is the difference of the superconducting phase across the Josephson junction. As discussed in more detail in the chapter by Konrad Lehnert and the chapter by Aaron O’Connell and Andrew Cleland, the corresponding quantum operators obey the standard commutation relations  $[\hat{N}, \hat{\delta}] = i$  and the Hamiltonian operator for the CPB is

$$\hat{H}_{\text{CPB}} = E_C (\hat{N} - N_g)^2 - E_J \cos(\hat{\delta}). \quad (14.6)$$

Here  $E_C = 4e^2/2C_\Sigma$  is the charging energy for a total island capacitance  $C_\Sigma$ ,  $E_J$  is the Josephson energy, and  $N_g = C_g V_g / (2e)$  the dimensionless gate charge which can be adjusted by the voltage  $V_g$  applied across the gate capacitance  $C_g$ . The CPB is usually operated in a regime where the charging energy  $E_C/h \sim 50$  GHz is the dominant energy scale and the dynamics of the CPB is restricted to the two energetically lowest charge states. For example, by setting  $N_g = n + 1/2 + \Delta N_g$  with integer  $n$  and  $\Delta N_g < 1$ , these two states are  $|g\rangle = |N = n\rangle$  and  $|e\rangle = |N = n + 1\rangle$  and form the basis of a so-called ‘charge qubit’ [26]. The states  $|g\rangle$  and  $|e\rangle$  are separated by an adjustable charging energy  $E_{eg} = 2E_C \Delta N_g$  and coupled by the Josephson tunneling term  $\langle g | \hat{H}_{\text{CPB}} | e \rangle = -E_J/2$ .

When the gate electrode is replaced by a vibrating mechanical beam the capacitance  $C_g(x) \approx C_g(1 - x/d)$  varies with the beam displacement  $x$  and the resulting change in the charging energy  $E_{eg}(x)$  introduces a coupling between the qubit states and the mechanical resonator. The Hamiltonian for the combined system is then given by [8, 9]

$$\hat{H} = E_C \Delta N_g \hat{\sigma}_z - \frac{E_J}{2} \hat{\sigma}_x + \hbar \Omega_M \hat{b}^\dagger \hat{b} + \hbar \lambda (\hat{b} + \hat{b}^\dagger) \hat{\sigma}_z, \quad (14.7)$$

and we recover the general form of Eq. (14.1) of the qubit-resonator coupling with a single phonon coupling constant  $\lambda \equiv \lambda_{el}$  as defined in Eq. (14.2). Due to the electrostatic nature of the interaction the achievable coupling strength  $\lambda_{el}/2\pi \sim 10$  MHz between a charge qubit and a mechanical resonator can be substantially larger than the corresponding magnetic interactions with spin qubits discussed in Sect. 14.2.3. However, for the same reason charge states are also more susceptible to random interactions with the environment and typical dephasing times  $T_2$  for charge superposition states are in the pico- to nanosecond regime. An exception to this rule occurs when the CPB is operated at the charge degeneracy point  $\Delta N_g = 0$ . Here the eigenstates of  $\hat{H}_{\text{CPB}}$ , namely  $|\tilde{g}\rangle = (|g\rangle + |e\rangle)/\sqrt{2}$  and  $|\tilde{e}\rangle = (|g\rangle - |e\rangle)/\sqrt{2}$ , are combinations of different charge states and therefore highly insensitive to ubiquitous sources of low frequency electric noise [27]. By assuming  $\Delta N_g = 0$  and re-expressing Eq. (14.7) in terms of the Pauli operators  $\tilde{\sigma}_j$  for the rotated basis states  $|\tilde{g}\rangle, |\tilde{e}\rangle$  we obtain

$$\hat{H} = \frac{E_J}{2}\tilde{\sigma}_z + \hbar\Omega_M\hat{b}^\dagger\hat{b} + \hbar\lambda(\hat{b} + \hat{b}^\dagger)\tilde{\sigma}_x, \quad (14.8)$$

as our final model for the coupled resonator charge-qubit system. Indeed, by using optimized charge qubit designs dephasing times  $T_2 > 1 \mu\text{s}$  have been demonstrated [27, 28]. This makes the CPB a promising candidate to achieve strong coupling  $\lambda T_2 > 1$  with a mechanical resonator.

Equation (14.8) is familiar from related models studied in the context of cavity QED [29] or trapped ions [30], where usually a resonant exchange of excitations between the qubit and the resonator is used for cooling or quantum control of the resonator mode. However, with the exception of the high frequency dilatation modes described in the chapter by Cleland et al., mechanical frequencies of  $\mu\text{m}$  sized beams are typically in the range of 10–100 MHz and Eq. (14.8) describes a highly non-resonant coupling to a qubit with a transition frequency  $E_J/h \sim 5$  GHz. Therefore, in the following we briefly outline two possibly strategies for potential quantum applications in the present system. First, we remark that in the relevant regime  $\lambda \ll \Omega_M < E_J$  second order perturbation theory can be used to approximate Eq. (14.8) by an effective Hamiltonian [9, 11]

$$\hat{H} \simeq \frac{E_J}{2}\tilde{\sigma}_z + \hbar\Omega_M\hat{b}^\dagger\hat{b} + \hbar\chi(\hat{b}^\dagger\hat{b} + 1/2)\tilde{\sigma}_z. \quad (14.9)$$

The resulting coupling term with a strength  $\hbar\chi = (\hbar\lambda)^2 \times 2E_J/(E_J^2 - (\hbar\Omega_M)^2)$  can be interpreted as a shift of the qubit frequency proportional to the phonon number  $\hat{b}^\dagger\hat{b}$ . Under the condition  $\chi T_2 > 1$  this frequency shift can in principle be detected and the charge qubit can be used to implement a quantum non-demolition measurement of the number of vibrational quanta of the mechanical mode. To resolve a single vibrational level in time the coupling  $\chi$  must also exceed the rate  $\Gamma_{\text{th}}$  at which the environment induces jumps between different vibrational states of the resonator. Estimates show that in this setting the combined condition  $\chi > \Gamma_{\text{th}}, T_2^{-1}$  for a phonon resolved measurement is experimentally feasible [9].

To go beyond passive measurement applications a second strategy is to realize effective resonance conditions by applying an oscillating gate voltage  $V_g(t) \sim \cos(\omega_0 t)$  such that the microwave frequency  $\omega_0 = E_J/\hbar - \Omega_M$  is used to gap the energy between vibrational and qubit excitations [10, 31]. In the interaction picture with respect to the free evolution  $\hat{H}_0 = E_J/2\tilde{\sigma}_z + \hbar\Omega_M\hat{b}^\dagger\hat{b}$  the resulting Hamiltonian is then of the form

$$\hat{H} \simeq \lambda(\tilde{\sigma}_+\hat{b} + \tilde{\sigma}_-\hat{b}^\dagger) + \mathcal{O}\left(e^{\pm i2\Omega_M t}, e^{\pm i2\omega_0 t}\right), \quad (14.10)$$

where for  $\lambda \ll \Omega_M, \omega_0$  the oscillating terms can be neglected by using a rotating wave approximation. Hamiltonian (14.10) reduces to the resonant Jaynes-Cummings model which allows a coherent exchange of qubit and vibrational excitations. Applications of this model such as sideband cooling, state preparation and detection have been discussed in different areas of quantum optics [32]. The driven CPB provides the tool to implement similar applications [10, 31] for the vibrational modes of macroscopic mechanical resonators. We close this section by noting that strong coupling of a superconducting phase qubit to a mechanical oscillator has been observed experimentally [33], as discussed in more detail in the chapter by O’Connell and Cleland.

### 14.2.3 Spin Qubits and Mechanics

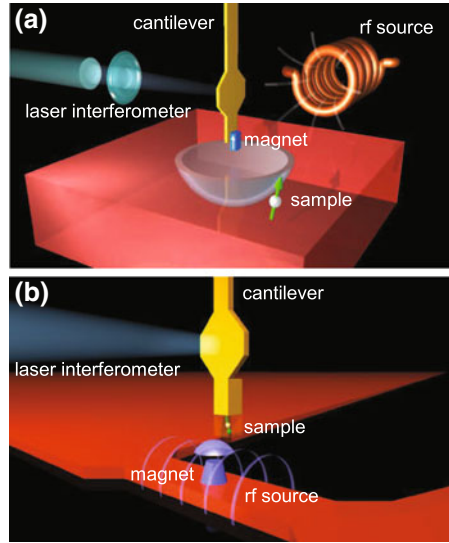
As discussed in Sect. 14.2.1, electronic and nuclear spin states can be coupled to mechanical motion by way of a magnetic field gradient. In the solid state, this situation is realized by positioning a spin qubit—typically residing in the lattice of some material—in close proximity to a strongly magnetized tip. One of the two elements, the tip or the qubit, is then rigidly affixed to a cantilever or other mechanical resonator. The most prominent examples of such experiments include mechanically detected magnetic resonance and optical experiments on nitrogen-vacancy defects in diamond.

#### 14.2.3.1 Mechanical Detection of a Single Electron Spin

The first experiments demonstrating coupling between a nanomechanical cantilever and the spin of an isolated single electron appeared in 2004. In a landmark experiment, Rugar et al. measured the force of flipping a single unpaired electron spin contained in a silicon dangling bond (commonly known as an E’ center) using a NEMS cantilever [19]. This achievement concluded a decade of development of a technique known as magnetic resonance force microscopy (MRFM) and stands out as one of the first single-spin measurements in a solid-state system.

The principle behind MRFM is simple (see Fig. 14.2). Magnetic moments—such as those associated with single electron or single nuclear spins—produce a force when in a magnetic field gradient:  $F = \mu \nabla B$ , where  $\mu$  is the spin’s magnetic moment and

**Fig. 14.2** Schematics of an MRFM apparatus. **a** “Tip-on-cantilever” arrangement, such as used in the single electron MRFM experiment of 2004 [19]. **b** “Sample-on-cantilever” arrangement, like the one used for the nanoscale virus imaging experiment in 2009 [20]. In both cases the hemispherical region around the magnetic tip is the region where the spin resonance condition is met—the so-called “resonant slice”



$\nabla B$  is the spatial field gradient. This force can couple the deflection of a compliant cantilever to the spin if either the spin or the gradient source, such as a small magnet, are fixed to the cantilever. If the magnetic field gradient is large enough (i.e. the coupling is strong enough), the spin polarization and the cantilever’s motion will be coupled.

Most MRFM techniques utilize this coupling to make measurements of spin density on the micro- or nanometer scale [34]. They employ extremely compliant cantilevers capable of detecting forces as small as  $1 \text{ aN}/\sqrt{\text{Hz}}$  and optical interferometers that can measure the cantilever’s displacement to resolutions of  $1 \text{ pm}/\sqrt{\text{Hz}}$ . Furthermore, magnetic resonance techniques are used in order to selectively address ensembles of spins in a sample, allowing for both spatial and chemical selectivity. For example, a pulse sequence known as a rapid adiabatic passage can be applied using a radio-frequency (rf) source. Each adiabatic passage pulse causes only the spins on resonance with the rf carrier frequency to flip. Using a periodic pulse sequence, a small ensemble of spins—at a particular region in space—can be made to flip at nearly any desired frequency. By choosing the flip frequency to be at the cantilever’s mechanical resonance, the periodic spin oscillations will in turn drive the cantilever into oscillation. Because this spin force is made to occur at the cantilever’s resonant frequency and at a particular phase, it can be distinguished from all other random electro-static and thermal forces disturbing the cantilever’s motion.

We should note that the force sensitivity required for the single electron spin measurement imposed several limitations. Since the single-shot signal-to-noise ratio (SNR) was 0.06, up to 12 h of averaging per data point were required [19]. In addition to making useful imaging prohibitively time-consuming, this small SNR precludes the technique from following the dynamics of the single electron spin. Large SNRs would allow for shorter measurement times. If the measurement time could

be reduced below the correlation time of the electron spin, which is related to the relaxation time of the electron spin in its rotating frame, real-time readout of the spin quantum state would become possible. Such readout would enable a wide variety of quantum measurement experiments. In the case of the electron spin E' centers, the correlation time was measured to be 760 ms. Until the SNR improves dramatically, real-time readout of spins will only be possible for small ensembles of electrons rather than for single electrons. One example is the real-time measurement of the direction of spin polarization for an ensemble of spins ( $\sim 70$  electron spins) [35]. In contrast, due to low SNR, the single-spin measurement [19] could not discern the direction of the measured spin; it could only ascertain its position.

### 14.2.3.2 Mechanical Detection of Nuclear Spins

Using this technique to couple and detect a single nuclear spin is far more challenging than to detect a single electron spin. The magnetic moment of a nucleus is much smaller than that of an electron: a  $^1\text{H}$  nucleus (proton), for example, possesses a magnetic moment that is only  $\sim 1/650$  of an electron spin moment. Since the measured force,  $F$ , is directly proportional to the magnetic moment of the spin, a significantly higher force resolution is required for nuclear spin experiments than for electron spin experiments. Other important nuclei, such as  $^{13}\text{C}$  or a variety of isotopes present in semiconductors, have even weaker magnetic moments than  $^1\text{H}$ . In order to observe single nuclear spins, it is necessary to improve the state-of-the-art sensitivity by another two to three orders of magnitude. While not out of the question, this is a daunting task that requires significant advances to all aspects of the MRFM technique.

### 14.2.3.3 Strong Magnetic Coupling

The strong magnetic coupling achieved between spins and the cantilever enables the high sensitivity of MRFM. This coupling is mediated by field gradients that can exceed  $5 \times 10^6$  T/m [23, 24]. For the cantilevers and magnetic tips used in these experiments this corresponds to  $\lambda_{mag}/2\pi \approx 10$  kHz for a single electron spin and 10 Hz for a proton. Such high gradients have been achieved using micro-fabricated Dy or FeCo magnetic tips and by the ability to make stable measurements with the sample positioned less than 50 nm from the apex of the tip. The strong interaction between spins and the mechanical sensor has been the subject of a number of theoretical studies, and is predicted to lead to a host of intriguing effects. These range from shortening of spin lifetimes by “back action” [36, 37], to spin alignment by specific mechanical modes either at the Larmor frequency or in the rotating frame [38], to a mechanical analog of a laser [18], and to long-range mediation of spin couplings using charged resonator arrays [39].

The first direct experimental evidence for accelerated nuclear spin relaxation induced by a single, low-frequency mechanical mode was reported in 2008 [40].

In these experiments the slight thermal vibration of the cantilever generated enough magnetic noise to destabilize the spin. Enhanced relaxation was found when one of the cantilever's upper modes (in particular the third mode with a frequency of about 120 kHz) coincided with the Rabi frequency of the  $^{19}\text{F}$  spins in  $\text{CaF}_2$ . In this regime, the spins are more tightly coupled to one mechanical resonator mode than to the continuum of phonons that are normally responsible for spin-lattice relaxation. Interestingly, these initial experiments showed a scaling behavior of the spin relaxation rate with important parameters, including magnetic field gradient and temperature, that is substantially smaller than predicted by theory.

#### 14.2.3.4 Nano-MRI and Potential Practical Applications

The coupling of small nuclear spin ensembles to a compliant mechanical oscillator through strong magnetic tips has resulted in the highest magnetic resonance imaging (MRI) resolution achieved by any method. In 2009, Degen et al. demonstrated three-dimensional (3D) MRI of  $^1\text{H}$  nuclear spins in a biological specimen (tobacco mosaic virus) with a spatial resolution down below 10 nm [20]. This resolution represents a 100 million-fold improvement in volume resolution over conventional MRI and shows the potential of MRFM as a tool for elementally selective imaging on the nanometer scale. If the development of such techniques continues, these results indicate that force-detected spin resonance has the potential to become a significant tool for structural biologists.

#### 14.2.3.5 Nitrogen Vacancy Centers and Mechanics

Recently, single nitrogen vacancy (NV) centers hosted in diamond have been proposed as solid-state qubits amenable to mechanical coupling [22]. Again, as in the case of MRFM, the coupling rests on bringing the qubit—in this case a single NV—in close proximity to a strongly magnetized tip. Then, either the NV or the tip must be affixed to a mechanical oscillator. NV centers appear especially attractive qubits due to their excellent optical and electronic properties. A single NV spin can be readily initialized and measured by optical means, manipulated using resonant rf pulses, and excellent coherence times up to a few milliseconds persist even in ambient conditions [41, 42]. As a result NVs have been proposed and used as ultra-sensitive scanning magnetic sensors [43–46].

First experiments have recently demonstrated the coupling of the NV spin to mechanical motion. Arcizet et al. coupled an NV to the motion of a SiC nanowire using field gradients around  $7 \times 10^3$  T/m [47]. The NV was fixed to the tip of the nanowire while the magnet was placed near to it. Nanowire vibrations of a few tens of nanometers in amplitude were detected through a change in the lineshape of the NV spin resonance. More recently, Kolkowitz et al. used an NV spin to sense the vibrations of a cantilever resonator with a magnetic tip [48]. A sequence of coherent manipulation pulses was applied to the spin in order to enhance its sensitivity to

the resonator vibrations while suppressing noise from other sources. In this way, mechanical vibrations down to a few picometers in amplitude were detected without phase locking NV spin dynamics and resonator vibrations. In these initial experiments, the spin-resonator coupling strength was  $\lambda_{mag}/2\pi = 70$  Hz [47] or lower [48]. Coupling strengths in the kHz range could be reached by combining a strong magnet with a nanoscale oscillator with large zero-point motion [48].

### 14.2.3.6 Increasing the magnetic coupling strength

The prospects of improving hybrid mechanical systems based on spin qubits depend on progress in increasing the magnetic coupling strength  $\lambda_{mag}$ . First, the magnetic tips can and must be improved with the use of cleaner materials and lithographic processing techniques. Second, the development of experimental techniques designed to bring the spin qubit and the gradient source as close together as possible without destroying either qubit coherence or introducing mechanical dissipation should also yield significant gains in coupling strength.

## 14.3 Atoms, Ions, and Molecules Coupled to Mechanics

Atoms, ions, and molecules are quantum systems par excellence, and a sophisticated toolbox exists for coherent manipulation of their electronic, spin, and motional degrees of freedom [49, 50]. It is therefore natural to ask whether such atomic quantum systems can be coupled to mechanical oscillators. Through the coupling, the tools of atomic physics could become available for quantum control of mechanical devices. On the other hand, mechanical oscillators could find new applications in atomic physics experiments, such as optical lattices with vibrating mirrors.

Compared to the solid-state based approaches discussed in the previous sections, coupling atomic systems to mechanical oscillators creates a qualitatively different setting. Atoms in a trap can be regarded as mechanical oscillators themselves. Acting as a dispersive medium inside an optical cavity, an interesting variant of cavity optomechanics in the quantum regime can be realized (see the chapter by Stamper Kurn). Atomic systems offer both the continuous degree of freedom of their motion in a trap as well as a discrete set of internal electronic and spin states that can be reduced to two-level systems. Both the internal and motional state can be initialized, coherently manipulated, and detected on the quantum level with high fidelity, using techniques that have been developed in experiments on atomic clocks and interferometers [51, 52], Bose-Einstein condensation [53–55], and quantum information processing [56]. Coherence times of atomic systems are typically in the range of milliseconds up to many seconds [57], and thus much longer than those of most solid-state quantum systems discussed in the previous sections. Moreover, many properties of atomic systems can be widely tuned in-situ with external fields, including trapping frequencies, laser cooling rates, and even the strength of atom–atom interactions.

While the good isolation of atoms trapped in a vacuum chamber enables long coherence times, it renders coupling to mechanical oscillators more challenging. Various coupling mechanisms have been proposed, such as electrostatic coupling to the motion of trapped ions [58–60] and molecules [61], magnetic coupling to atomic spins [62–66], and optomechanical coupling to atoms in free space [67–69] and in optical cavities [70–80]. Remarkably, some of these schemes predict strong atom-oscillator coupling even for a single atom [73, 74]. First experimental implementations of hybrid atom-oscillator systems have recently been reported [81–84]. In the following, we discuss several of these proposals and experiments (see also the review in [85]).

### 14.3.1 Direct Mechanical Coupling

The conceptually most straightforward approach is to directly couple the vibrations of a mechanical oscillator to the vibrations of an atom or ion in a trap with the help of a “spring”, i.e. a distance-dependent force between the two systems [85]. We consider an atom of mass  $m_{at}$  in a trap of frequency  $\Omega_{at}$  and a mechanical oscillator of mass  $m_{\text{eff}}$  and frequency  $\Omega_M$ . The coupling force derives from a potential  $U_c(d)$  that depends on the distance  $d$  between the oscillator and the atom. For small displacements  $\hat{x}$ ,  $\hat{x}_{at} \ll d$ , the resulting coupling Hamiltonian is of the form  $\hat{H}_c = U_c''(d)\hat{x}\hat{x}_{at}$ , where  $U_c''(d)$  is the curvature of  $U_c$  evaluated at the mean atom-oscillator distance  $d$ . The oscillator displacement can be written as  $\hat{x} = x_{\text{ZPF}}(\hat{b} + \hat{b}^\dagger)$  in terms of creation/annihilation operators  $[\hat{b}, \hat{b}^\dagger] = 1$  and the zero-point amplitude  $x_{\text{ZPF}} = \sqrt{\hbar/2m_{\text{eff}}\Omega_M}$ . Similarly, the atomic displacement is  $\hat{x}_{at} = x_{at,0}(\hat{a}_{at} + \hat{a}_{at}^\dagger)$  with  $[\hat{a}_{at}, \hat{a}_{at}^\dagger] = 1$  and  $x_{at,0} = \sqrt{\hbar/2m_{at}\Omega_{at}}$ . The Hamiltonian of the coupled system is then given by

$$\hat{H} = \hbar\Omega_{at}\hat{a}_{at}^\dagger\hat{a}_{at} + \hbar\Omega_M\hat{b}^\dagger\hat{b} + \hbar\lambda(\hat{a}_{at} + \hat{a}_{at}^\dagger)(\hat{b} + \hat{b}^\dagger), \quad (14.11)$$

with a single-phonon atom-oscillator coupling constant

$$\hbar\lambda = U_c''(d)x_{\text{ZPF}}x_{at,0} \simeq \varepsilon \frac{\hbar\Omega_{at}}{2} \sqrt{\frac{m_{at}}{m_{\text{eff}}}}, \quad (14.12)$$

for near-resonant coupling  $\Omega_{at} \simeq \Omega_M$ . It is important to note that  $U_c$  also modifies the atomic trapping potential by contributing a term of order  $U_c''(d)\hat{x}_{at}^2$  [85]. We therefore introduce the dimensionless parameter  $\varepsilon = U_c''(d)/(m_{at}\Omega_{at}^2)$ , which compares  $U_c''(d)$  to the curvature of the atom trap. To avoid strong trap distortion, we typically have  $\varepsilon \ll 1$ . In the special case where  $U_c$  itself provides the atom trap, we have  $\varepsilon = 1$ . To achieve  $\varepsilon > 1$ , the effect of  $U_c$  on the trap has to be partially compensated, requiring sophisticated trap engineering. For direct mechanical coupling, we thus find that  $\lambda$  scales with  $\Omega_{at}$  but is reduced by the atom-oscillator mass ratio, which is typically

very small ( $\sqrt{m_{at}/m_{\text{eff}}} \sim 10^{-8} - 10^{-4}$ ). To achieve significant coupling strength, oscillators with small  $m_{\text{eff}}$  are advantageous.

Several theoretical proposals consider direct mechanical coupling between a trapped ion and an oscillator with a metallic electrode on its tip [58–60]. In this case,  $U_c = eq/(4\pi\epsilon_0 d)$  is the Coulomb interaction between the ion of elementary charge  $e$  and the charge  $q = C_q V_q$  on the oscillator tip. For a nanoscale oscillator with  $m_{\text{eff}} = 10^{-15}$  kg coupled to a single  ${}^9\text{Be}^+$  ion in a trap with  $\Omega_{at}/2\pi = 70$  MHz, we obtain  $\lambda/2\pi = \epsilon \times 150$  Hz assuming  $\Omega_M = \Omega_{at}$  [85]. A value of  $\epsilon = 1$  can be achieved e.g. with  $d = 10$   $\mu\text{m}$  and a metallic tip with a capacitance  $C_q = 10^{-17}$  F and an applied voltage  $V_q = 90$  V.

Stronger coupling is possible if  $N \gg 1$  atoms are simultaneously coupled to the mechanical oscillator. In this case,  $\hat{a}_{at}$  and  $\hat{a}_{at}^\dagger$  refer to the atomic center-of-mass (COM) motion. The coupling is collectively enhanced by a factor  $\sqrt{N}$ , so that

$$\lambda_N = \lambda\sqrt{N} = \epsilon \frac{\Omega_{at}}{2} \sqrt{\frac{Nm_{at}}{m_{\text{eff}}}}. \quad (14.13)$$

This result can be intuitively obtained by replacing  $m_{at} \rightarrow Nm_{at}$  in Eq. (14.12), for a derivation see [68]. An example of such collective coupling where  $\lambda_N$  can reach several kHz is given in Sect. 14.3.3.

In the experiment of [82], a direct mechanical coupling between a cantilever oscillator and ultracold atoms was demonstrated for the first time. An atomic Bose-Einstein condensate (BEC) of  $N = 2 \times 10^3$  atoms was placed at about one micrometer distance from the surface of the cantilever and used as a probe for cantilever oscillations (see Fig. 14.3a). The coupling potential  $U_c$  is due to attractive atom-surface interactions, which substantially modify the magnetic trapping potential  $U_m$  at such small distance. One effect of the surface force is to reduce the potential depth (see Fig. 14.3b). In addition, it shifts the trap frequency and minimum position. When the cantilever oscillates, the trapping potential is modulated at the cantilever frequency  $\Omega_M$ , resulting in mechanical coupling to the atoms as described above.

In the experiment, the vibrating cantilever induced large-amplitude atomic motion that was detected simply via atom loss across the barrier  $U_0$ , see Fig. 14.3c. The observed atom-cantilever coupling depends strongly on the trap parameters and shows resonant behavior if  $\Omega_M = \Omega_{at}$ . Coupling to collective mechanical modes of the BEC other than the COM mode was observed as well [82]. While it was possible to detect the cantilever motion with the atoms, the backaction of atoms onto the cantilever was negligible in this experiment, mainly because the relatively large  $m_{\text{eff}} = 5$  ng results in a small coupling constant  $\lambda_N/2\pi \simeq 10^{-2}$  Hz. Much stronger coupling could be achieved by miniaturizing the cantilever. Since coupling via surface forces does not require functionalization of the cantilever, it could be used to couple atoms to molecular-scale oscillators such as carbon nanotubes [86]. In this case, a coupling constant of a few hundred Hz could be achieved [85].

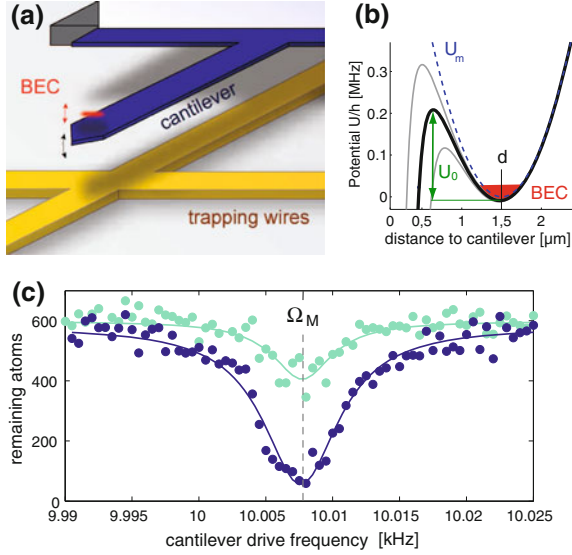


**Fig. 14.3** Coupling of a mechanical cantilever and an atomic BEC via atom-surface forces [82]. **a** Atom chip with cantilever oscillator (length  $200\ \mu\text{m}$ ,  $\Omega_M/2\pi = 10\ \text{kHz}$ ,  $m_{\text{eff}} = 5\ \text{ng}$ ,  $Q = 3,200$ ). The atoms can be trapped and positioned near the cantilever with magnetic fields from wire currents. **b** Combined magnetic trapping and surface potential. The surface potential reduces the trap depth to  $U_0$ . Cantilever oscillations modulate the potential, thereby coupling to atomic motion. **c** Cantilever resonance detected with the atoms, for two different driving strengths of the cantilever

### 14.3.2 Magnetic Coupling to Atomic Spin

The vibrations of a mechanical oscillator can also be coupled to the spin of the atoms. This has several advantages compared to coupling to atomic motion. First, the atomic spin can be manipulated with higher fidelity. For hyperfine spins, coherence times  $T_2$  of many seconds have been achieved [57]. Second, it is easier to isolate a two-level system among the internal states, providing a way to the preparation of non-classical quantum states of the oscillator. Third, hyperfine spin transition frequencies lie in the MHz to GHz range, significantly higher than typical trap frequencies. This enables coupling to high-frequency mechanical oscillators, which are easier to cool to the ground state.

To couple to the spin of the atoms, the oscillator is functionalized with a small magnet that generates a field gradient  $\nabla B$ , see Fig. 14.4a. Mechanical oscillations  $x(t)$  are transduced into an oscillating magnetic field  $B_r(t) = \nabla B x(t)$  that couples to the spin. If  $B_r(t)$  is perpendicular to the static field  $B_0$  in the trap, the Hamiltonian is

$$\hat{H} = \frac{\hbar\omega_L}{2}\hat{\sigma}_z + \hbar\Omega_M\hat{b}^\dagger\hat{b} + \hbar\lambda_{\text{mag}}(\hat{b} + \hat{b}^\dagger)\hat{\sigma}_x \quad (14.14)$$

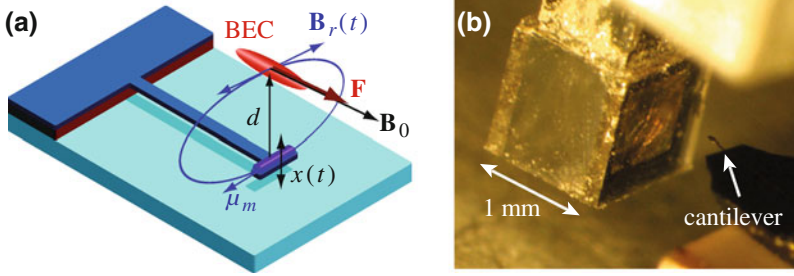


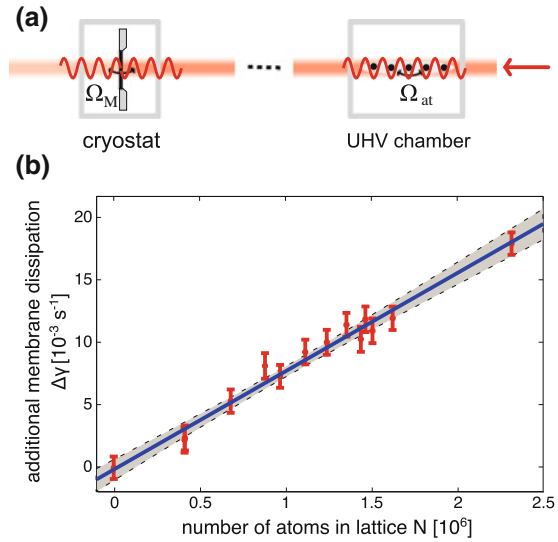
**Fig. 14.4** **a** Schematic setup for coupling the spin of an atomic BEC to a nanoscale cantilever with a magnetic tip [62]. Cantilever oscillations  $x(t)$  are transduced by the magnet into an oscillating field  $B_r(t)$ , which couples to the spin  $F$  of the atoms. **b** Experimental setup of [81], where a vibrating cantilever with a magnetic tip induces atomic spin resonance in a room-temperature Rb vapor cell

with a coupling constant  $\lambda_{mag} = g\mu_B x_{ZPF} \nabla B / 2\hbar$  similar to Eq. (14.4). The prefactor  $g$  (of order unity) accounts for the matrix element of the atomic hyperfine transition considered. For transitions between Zeeman sublevels, the Larmor frequency is  $\omega_L = g_F \mu_B B_0 / \hbar$ , with the hyperfine Landé factor  $g_F$ . It can be widely tuned by adjusting  $B_0$  in order to achieve resonance  $\omega_L = \Omega_M$ . The coupled system realizes a mechanical analog of the Jaynes-Cummings model in cavity quantum electrodynamics [29], with the *phonons* of the mechanical oscillator playing the role of the *photons* of the electromagnetic field.

To achieve large  $\lambda_{mag}$  a strong gradient  $\nabla B$  is required. Approximating the magnet by a dipole of magnetic moment  $\mu_m$ , we have  $\nabla B = 3\mu_0 \mu_m / 4\pi d^4$ . It is thus essential to trap and position the atoms at very small distance  $d$  from the oscillator tip. At the same time, care has to be taken that  $\nabla B$  does not significantly distort the atomic trapping potential. With neutral atoms in magnetic microtraps,  $d$  can be as small as a few hundred nanometers [82]. Compared with the solid-state implementations discussed in Sect. 14.2.3, where  $d$  can be in the tens of nanometers range, it is thus more difficult to achieve large  $\nabla B$ . On the other hand, the spin decoherence rates  $T_2^{-1}$  of trapped atoms are exceptionally small. The main challenge is the thermal decoherence rate  $\Gamma_{th} = k_B T / \hbar Q$  of the mechanical oscillator. The single-phonon single-atom strong coupling regime requires  $\lambda_{mag} > \Gamma_{th}, T_2^{-1}$ . As in the previous section, collective coupling to  $N \gg 1$  atoms is a possible strategy to enhance the coupling strength. In this case, the collective strong-coupling regime requires  $\lambda_N = \lambda_{mag} \sqrt{N} > \Gamma_{th}, T_2^{-1}$ . Several theory papers investigate how to achieve the strong coupling regime by coupling nanoscale cantilevers to the spin of ultracold neutral atoms [62–66]. The predicted coupling constants lie in the range of  $\lambda/2\pi \approx 10 - 10^3$  Hz, so that very high  $Q$  and low  $T$  are required for strong coupling.

In [81], a first experiment was reported where a cantilever with a magnetic tip was coupled to atoms in a room-temperature vapor cell, see Fig. 14.4b. The cantilever was piezo-driven and induced spin resonance in the atomic vapor, which was recorded with a laser. Besides demonstrating spin-oscillator coupling, such a setup is of interest for applications in magnetic field sensing, where the cantilever is essentially used as a tool for spectroscopy of the atomic transition frequency.

**Fig. 14.5** **a** Setup: Reflection of light from a micromechanical membrane results in a standing wave which provides an optical lattice potential for ultracold atoms. This configuration gives rise to a coupling of the membrane vibrations and the center of mass motion of the cloud of atoms. Laser cooling of atoms will sympathetically cool along the membrane [68]. **b** Measured change in the mechanical damping rate due to the sympathetic cooling effect in its dependence on atom number in the lattice [83]



### 14.3.3 Optomechanical Coupling in Free Space

The coupling mechanisms discussed in the preceding sections require to position atoms close to the mechanical oscillator. Combining trapping and cooling of atoms in ultra-high vacuum (UHV) with a cryogenic environment as required for minimizing decoherence of the micromechanical system is a demanding task. In contrast, an indirect coupling mechanism acting over some distance would allow to keep the atomic and the micromechanical system in separate environments. Such a scheme was suggested in [68, 69] and experimentally implemented as described in [83, 84].

Consider the setup shown in Fig. 14.5a. Laser light is retroreflected from a partially reflective membrane, resulting in a standing wave light field, which in turn provides an optical lattice potential for a cloud of cold atoms. When the membrane supports a mechanical degree of freedom its position fluctuations will move the optical lattice, and thereby shake along the atoms. Conversely, position fluctuations of atoms in the potential will couple to the membrane's motion: When an atom is displaced from its potential minimum it will experience a restoring force which is due to transfer of photon momentum to the atom. This change in photon momentum is caused by an unbalancing of power between left and right propagating beams, which ultimately changes also the radiation pressure force on the membrane. Thus, also the membrane vibrates along with the atoms.

A more quantitative, semi-classical consideration along these lines reveals that the (dimensionless) position and momentum fluctuations of the membrane and the atomic COM motion,  $\hat{q} = (\hat{b} + \hat{b}^\dagger)/\sqrt{2}$ ,  $\hat{p} = i(\hat{b}^\dagger - \hat{b})/\sqrt{2}$  and  $\hat{q}_{at} = (\hat{a}_{at} + \hat{a}_{at}^\dagger)/\sqrt{2}$ ,  $\hat{p}_{at} = i(\hat{a}_{at}^\dagger - \hat{a}_{at})/\sqrt{2}$ , respectively, *on average* obey the equations of motion

$$\begin{aligned}\dot{\langle \hat{p} \rangle} &= -\Omega_M \langle \hat{q} \rangle - 2r\lambda_N \langle \hat{q}_{at} \rangle, & \dot{\langle \hat{q} \rangle} &= \Omega_M \langle \hat{p} \rangle, \\ \dot{\langle \hat{p}_{at} \rangle} &= -\Omega_{at} \langle \hat{q}_{at} \rangle - 2\lambda_N \langle \hat{q} \rangle, & \dot{\langle \hat{q}_{at} \rangle} &= \Omega_{at} \langle \hat{p}_{at} \rangle.\end{aligned}\quad (14.15)$$

Here  $\Omega_{at}$  denotes the trap frequency for atoms provided by the optical potential,  $\lambda_N$  is the coupling strength between the COM motion of atoms and the membrane, and  $r$  is the power reflectivity of the membrane. The semiclassical calculation yields a coupling strength of  $\lambda_N = (\Omega_{at}/2)\sqrt{Nm_{at}/m_{\text{eff}}}$  as in Eq. (14.13), assuming resonance between the two systems  $\Omega_M = \Omega_{at}$ . For mechanical frequencies on the order of several 100 kHz this condition is routinely met in state of the art optical lattices. As expected from the discussion in Sect. 14.3.1 the coupling scales with the mass ratio between an atom and the membrane  $m_{at}/m_{\text{eff}}$ , but it is also collectively enhanced by the number of atoms  $N$ . Therefore even for a mass ratio  $m_{at}/m_{\text{eff}} \simeq 10^{-14}$ , a large but feasible atom number  $N = 10^8$  will still give rise to an appreciable coupling  $\lambda_N$  on the order of kHz for a trap frequency around one MHz. Moreover, it was recently shown that  $\lambda_N$  can be further increased by placing the membrane inside an optical cavity [69]. Since the atoms are still trapped in the optical lattice forming *outside* the cavity, the long-distance nature of the coupling is maintained.

Curiously, the semiclassical consideration outlined above predicts a coupling between atoms and membrane that is stronger in one direction than in the other by a factor given by the power reflectivity  $r$ . This scaling is in fact confirmed and explained by a full quantum treatment of this system. Starting from a complete Hamiltonian description including the motional degree of freedom of the membrane and atoms, as well as the quantized electromagnetic field, it is possible to derive a master equation for the density matrix  $\hat{\rho}$  of the membrane and atomic COM motion [68]. It has the form

$$\dot{\hat{\rho}} = -i[\hat{H}_{\text{sys}} - 2\lambda_N \hat{q}_{at} \hat{q}, \hat{\rho}] + C\hat{\rho} + L_m \hat{\rho} + L_{at} \hat{\rho}. \quad (14.16)$$

and implies the equations of motion (14.15) for the mean values. The term  $C\hat{\rho} = -i(1-r)\lambda_N([\hat{q}, \hat{q}_{at}\hat{\rho}] - [\hat{\rho}\hat{q}_{at}, \hat{q}])$  is responsible for the asymmetric coupling. Its form is well known in the theory of *cascaded quantum systems* [87, 88], and arises here due to the finite reflectivity of the membrane. The Lindblad terms  $L_m \hat{\rho}$  and  $L_{at} \hat{\rho}$  correspond to momentum diffusion of, respectively, the membrane and the atomic COM motion. They arise due to vacuum fluctuations of the radiation field giving rise to fluctuations of the radiation pressure force on the membrane and the dipole force on atoms. The full quantum treatment of the system correctly reproduces these well known effects, and shows that the corresponding diffusion rates are well below the rates of other relevant decoherence processes in this system: For the membrane mode this is thermal heating at a rate  $\Gamma_{\text{th}}$  due to clamping losses or absorption of laser light, which will heat the mechanical mode to thermal occupation  $\bar{n}_{\text{th}}$  in equilibrium. Atoms on the other hand can be *laser cooled* to the motional ground state by well established techniques such as Raman sideband cooling [83]. The corresponding cooling rate  $\gamma_{at, \text{cool}}$  is widely tunable and can in fact be significantly larger than  $\Gamma_{\text{th}}$ . Note that in contrast to the normal optomechanical situation the cooling rate of atoms can be *switched off* giving rise to a regime of coherent coupling between atoms and the membrane.

This opens up the interesting possibility to *sympathetically cool* the membrane motion via laser cooling of atoms in the lattice. Adding a corresponding heating term for the membrane and a cooling term for atoms to the master equation (14.16), and solving for the steady state it is possible to determine the effect of the atom-membrane coupling and the associated sympathetic cooling. In [68] it was shown that ground state cooling might in fact be within reach. In the weak coupling regime  $\lambda_N \ll \gamma_{at,cool}$  we expect in analogy to the treatment of optomechanical sideband cooling that laser cooling of atoms results in an increased effective mechanical damping rate  $\Gamma_{\text{eff}} = \Gamma_M + 4r\lambda_N^2/\gamma_{at,cool}$ , where  $\Gamma_M = \Omega_M/Q$  is the intrinsic damping rate of the membrane. Such an increase was observed in the experiment reported in [83]. Figure 14.5b shows the results for the change in mechanical damping  $\Delta\gamma = \Gamma_{\text{eff}} - \Gamma_M$  for various experiments with different number of atoms  $N$  in the lattice. The linear scaling as expected from the model discussed here is clearly confirmed. Also the magnitude of  $\Delta\gamma$  in the experiment agrees well with the prediction by this model.

Overall this setup provides exciting first results and perspectives for interfacing micromechanical oscillators with ultracold atoms. The interface works at a distance, easing experimental requirements, and enables sympathetic cooling towards the ground state, as well as coherent dynamics for quantum state preparation and measurement of the mechanical mode via coupling to ultracold atoms.

### 14.3.4 Cavity-Optomechanical Coupling Schemes

The optomechanical coupling discussed in the previous section can be enhanced by placing the atoms and the oscillator inside a high-finesse optical cavity. In such a system, the cavity field can mediate an interaction between the internal or motional degrees of freedom of the atoms and the vibrations of the oscillator. In the following, we first discuss a scheme where the oscillator interacts with the internal state of an atomic ensemble. Subsequently, we present a system where the motion of a single trapped atom is strongly coupled to a membrane oscillator.

#### 14.3.4.1 Coupling of Atomic Internal Levels to Resonator Motion

The presence of an ensemble of  $N$  two-level atoms inside a driven optical cavity modifies the cavity response. For example when the atomic resonance is far from the cavity mode frequency, i.e. in the dispersive limit, the effect of the atoms onto the field is a phase shift. Similarly a vibrating cavity end-mirror also leads to a phase shift of the intracavity field. The field can then be used as a mediator between atoms and the mechanical resonator to either allow an exchange of quantum states, entangle the two systems, or lead to enhanced optical cooling of the mirror. The last motive will be explored in the following and it can be seen as an atom induced effect of spectral filtering of the mirror scattered optical sidebands. The upshot is that low finesse

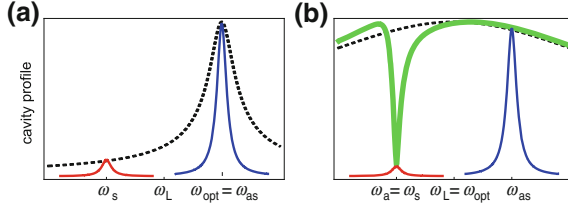


**Fig. 14.6** Resolved sideband cooling of an end-mirror **a** using a sharp resonance optical cavity and **b** using a bad-cavity with an ensemble of atoms inside. The *dotted black lines* show the empty cavity response while the *red* and *blue curves* represent optical sidebands. The *green line* shows the modification of the cavity response in the presence of atoms

cavities can provide resolved sideband cooling when supplemented with filtering ensembles of atoms [76].

The total Hamiltonian of the system can be split as  $\hat{H} = \hat{H}_0 + \hat{H}_I + \hat{H}_{dis}$ , where  $\hat{H}_0$  and  $\hat{H}_I$  are the free part and the interaction term, while  $\hat{H}_{dis}$  describes dissipation. The mirror quadratures are defined as above,  $\hat{q} = (\hat{b} + \hat{b}^\dagger)/\sqrt{2}$  and  $\hat{p} = i(\hat{b}^\dagger - \hat{b})/\sqrt{2}$ , and the atomic ensemble of frequency splitting  $\omega_a$  is described by creation/annihilation operators  $[\hat{c}, \hat{c}^\dagger] = 1$ . The atom-cavity coupling  $G_a = g_a\sqrt{N}$  is collectively enhanced by  $\sqrt{N}$  compared to the single atom-single photon coupling strength  $g_a$ . The harmonic oscillator description for the atomic cloud is accurate when the cavity photons are much less numerous than atoms  $\bar{n}_{cav} \ll N$ . The cavity resonance is  $\omega_{opt}$  and the laser driving shows up in  $\hat{H}_I$  as a displacement term of amplitude  $\mathcal{E} = \sqrt{2P_{in}\kappa/\hbar\omega_L}$ . One can derive equations of motion from the Hamiltonian dynamics and then perform a linearization of fluctuations around steady state values that leads to a set of quantum linearized Langevin equations

$$\dot{\hat{q}} = \Omega_M \hat{p}, \quad (14.17)$$

$$\dot{\hat{p}} = -\Gamma_M \hat{p} - \Omega_M \hat{q} + g(\hat{a} + \hat{a}^\dagger) + \xi, \quad (14.18)$$

$$\dot{\hat{a}} = -(\kappa + i\Delta_f)\hat{a} + ig\hat{q} - iG_a\hat{c} + \hat{a}_{in}, \quad (14.19)$$

$$\dot{\hat{c}} = -(\gamma_a + i\Delta_a)\hat{c} - iG_a\hat{a} + \hat{c}_{in}, \quad (14.20)$$

where  $\Delta_f = \omega_{opt} - \omega_L - g^2/\Omega_M$  is the effective cavity detuning,  $\kappa$  is the cavity decay rate,  $\gamma_a$  and  $\Delta_a = \omega_a - \omega_L$  are the atom decay rate and detuning respectively, and  $\xi$ ,  $\hat{a}_{in}$ ,  $\hat{c}_{in}$  is quantum noise describing the effect of  $\hat{H}_{dis}$  in the Langevin approach.

Setting  $G_a = 0$  we recover the typical resolved sideband regime in optomechanics where under the conditions  $\kappa \ll \Omega_M$  and  $\Delta_f = \Omega_M$ , optimal cooling of the mirror via the field is obtained as illustrated in Fig. 14.6a. The scattered sidebands are at  $\omega_{as,s} = \omega_L \pm \Omega_M$  and the sharp response of the cavity around  $\omega_{opt}$  leads to a suppression of the heating sideband. Assuming a bad cavity that cannot resolve sidebands and  $G_a > 0$ , we are instead in the situation depicted in Fig. 14.6b where the atoms, placed at  $\Delta_a = -\Omega_M$ , induce a dip in the cavity profile at  $\omega_s$  that inhibits scattering into the Stokes sideband. Defining atomic cooperativity  $C = G_a^2/\kappa\gamma_a$ , the

dip at  $\omega_s$  scales as  $(1 + C)^{-1}$ . The width of the dip is  $\gamma_a(1 + C)$  representing the enhanced light-induced atomic linewidth. When the Stokes sideband fits inside the dip one expects an inhibition by a factor of the order of  $(1 + C)^{-1}$ . For a rigorous analysis one analyzes the spectrum of the Langevin force  $\hat{F} = g(\hat{a}_{in} + \hat{a}_{in}^\dagger)$  which gives the cooling and heating rates (for  $\Delta_f = 0$ ):  $A_{as} \simeq g^2/\kappa$  and  $A_s \simeq g^2/[\kappa(1 + C)]$ . Subsequently, the effective atom-mediated optical damping is

$$\Gamma_{\text{opt}} = \frac{g^2}{\kappa} \frac{C}{1 + C}. \quad (14.21)$$

The residual occupancy is given by  $n^{\text{res}} = A_s/(\Gamma_M + \Gamma_{\text{opt}}) \rightarrow C^{-1}$  (in the limit of large  $C$ ) and can be compared with  $n^{\text{res}} = (\kappa/2\Omega_M)^2$  for the purely optomechanical system; an immediate advantage of this hybrid system comes from the scaling of  $n^{\text{res}}$  with the controllable parameter  $N$ .

While in the above the atomic system has been viewed rather as a high-Q system that acts as a spectral filter for light to relax the resolved sideband limit requirements, we nevertheless stress that one can as well take a different stand by seeing the cavity mode rather as a mediator between atoms and mechanical resonator. From here, following the elimination of the cavity field as a fast variable, one can also derive the exact form of the implicit atom-mirror interaction and show effects such as a quantum state swap or entanglement [71].

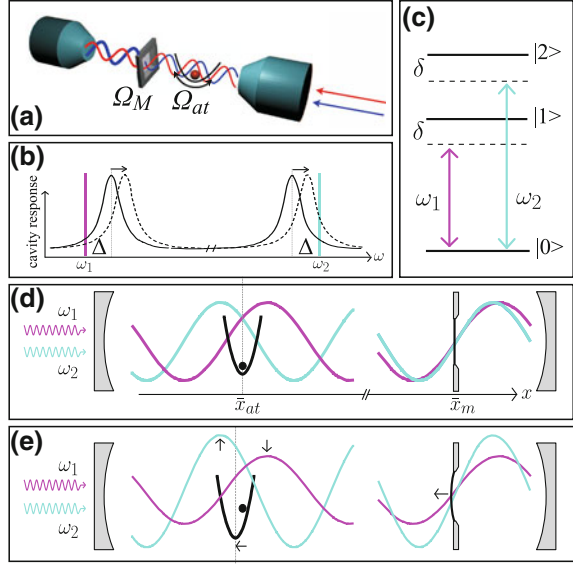
#### 14.3.4.2 Coupling of Atomic Motion to Resonator Motion

In a situation as that depicted in Fig. 14.7a, where a single atom is trapped inside a cavity that surrounds a vibrating membrane, the effect of light on atomic motion can be exploited to generate motion-motion coupling between membrane and atom [73, 74]. To this purpose we choose two fields of slightly different wavelengths and opposite detunings  $\pm\Delta$  with respect to two cavity resonances (see Fig. 14.7b) that provide harmonic trapping of the atom. The two fields have frequencies  $\omega_1, \omega_2$  equally far-detuned by  $\delta$  from two internal transitions of the atom as shown in Fig. 14.7c. Around the atomic equilibrium position  $\bar{x}_{at}$  a Lamb-Dicke expansion leads to a linear atom-field interaction

$$\hat{H}_{at,f} = g_{at,f}[(\hat{a}_1 + \hat{a}_1^\dagger) - (\hat{a}_2 + \hat{a}_2^\dagger)](\hat{a}_{at} + \hat{a}_{at}^\dagger), \quad (14.22)$$

where the atom-field coupling  $g_{at,f}$  as well as the atomic trapping frequency  $\Omega_{at}$  inside the two-field optical trap are quantities depending on the single-photon Stark shift, cavity photon number and the geometry of the fields at position  $\bar{x}_{at}$ . This interaction can be interpreted as follows (Fig. 14.7d, e): fluctuations in the amplitudes of the two cavity fields exert oppositely oriented forces on the atom. Conversely, fluctuations of the atom around its mean position cause changes of opposite sign

**Fig. 14.7** Linear atom-membrane coupling mediated by two driven cavity modes. **a** Schematics of the setup with atom, membrane and two cavity fields shown. **b** Two cavity resonances and the frequency position of the driving lasers. **c** Internal structure of the atom. **d** Static illustration of optical potentials. **e** Dynamical illustration of potentials showing the modification induced by motion of atom and membrane



in the amplitudes of the two cavity fields. The membrane-field interaction takes a similar form

$$\hat{H}_{m,f} = g_{m,f}[(\hat{a}_1 + \hat{a}_1^\dagger) - (\hat{a}_2 + \hat{a}_2^\dagger)](\hat{b} + \hat{b}^\dagger), \quad (14.23)$$

with a similar interpretation. To the reversible Hamiltonian dynamics one has of course to add the dissipation channels: cavity decay, momentum diffusion owing to spontaneous scattering of the atom and thermal decoherence of the membrane.

The elimination of the fast varying cavity fields can be done in the limit  $|\Delta| \gg g_{at,f}, g_{m,f}$ , and the reduced atom-membrane dynamics is governed by a linear two-mode Hamiltonian

$$\hat{H}_{at,m} = \Omega_M \hat{b}^\dagger \hat{b} + \Omega_{at} \hat{a}_{at}^\dagger \hat{a}_{at} - \lambda (\hat{a}_{at} + \hat{a}_{at}^\dagger) (\hat{b} + \hat{b}^\dagger), \quad (14.24)$$

with atom-membrane coupling strength

$$\lambda = \frac{2g_{at,f}g_{m,f}(\Delta + \Omega_M)}{\kappa^2 + (\Delta + \Omega_M)^2} + \frac{2g_{at,f}g_{m,f}(\Delta - \Omega_M)}{\kappa^2 + (\Delta - \Omega_M)^2}, \quad (14.25)$$

to which decoherence at rates  $\Gamma_c$ ,  $\Gamma_{at}$  and  $\Gamma_{th}$  adds irreversible dynamics.

The goal is to obtain a coupling  $\lambda$  much larger than the rates of decoherence. For a demonstrative example we consider a single Cs atom and a SiN membrane of small effective mass  $m_{\text{eff}} = 0.4 \text{ ng}$  inside a cavity of finesse of  $\mathcal{F} \simeq 2 \times 10^5$ . A small cavity waist of  $w_0 = 10 \text{ } \mu\text{m}$  results in a cooperativity parameter of 140. With a mechanical

quality factor  $Q = 10^7$ , resonance frequency  $\Omega_M = 2\pi \times 1.3$  MHz, circulating power  $P_c \simeq 850 \mu\text{W}$  and cavity length  $L = 50 \mu\text{m}$  we find a cavity mediated coupling  $\lambda \simeq 2\pi \times 45$  kHz and decoherence rates  $\Gamma_c, \Gamma_{\text{th}}, \Gamma_{\text{at}} \simeq 0.1 \times \lambda$ . It is thus possible to enter the strong coupling regime with state-of-the-art experimental parameters, even with just a single atom in the cavity.

## 14.4 Conclusion and Outlook

We have discussed various hybrid systems in which a mechanical oscillator is coupled to another (microscopic) quantum system. The approaches that are being pursued are quite diverse, involving superconducting qubits, single spins in the solid state, quantum dots, ultracold atoms in magnetic and optical traps, as well as trapped ions and molecules. One motivation for building such hybrid systems is that they enable novel ways to read out and control mechanical objects. For example, a switchable, linear coupling of a mechanical oscillator to a two-level system allows for the preparation of arbitrary quantum states of the oscillator through the Law-Eberly protocol [89].

Experimentally, the coupling of superconducting two-level systems to mechanical oscillators is most advanced. First experiments have already reached the strong-coupling regime (see [33] and the chapter by O’Connell and Cleland). However, the coherence time of the involved qubits is very short (nano- to microseconds), and it is thus highly desirable to develop and implement strategies for strong coupling of mechanical oscillators to long-lived qubits such as spins in the solid-state or ultracold atoms in a trap. Strong coupling of mechanical oscillators to solid-state spins can build on the impressive achievements of magnetic resonance force microscopy, which has reached single-spin detection sensitivity already some time ago [19]. Recently, a novel system was realized in which the spin of a nitrogen vacancy center in diamond was used to sense mechanical motion [47, 48]. In another recent experiment, an ensemble of ultracold atoms in an optical lattice was optically coupled to vibrations of a micromechanical membrane [83, 84], enabling sympathetic cooling of the membrane through laser-cooled atoms. By enhancing the coupling with a high-finesse cavity, strong coupling could be achieved even for a single atom [73].

The fact that very different microscopic quantum systems are investigated as potential candidates for strong coupling to mechanical oscillators points to one of the big strengths of mechanical quantum systems: the oscillator can be functionalized with electrodes, magnets, or mirrors while maintaining high mechanical quality factor. Mechanical oscillators are thus particularly well suited to serve as quantum transducers [39] for precision sensing or hybrid quantum information processing [90]. Through the mechanical vibrations, spin dynamics can e.g. be transduced into electric or optical signals, and one can envision scenarios where atomic quantum memories are interfaced with superconducting quantum processors. Another important application is the transduction of microwave or radio-frequency signals

into optical signals [91, 92], ultimately at the level of single quanta [93, 94]. The versatility of mechanical devices makes them a fascinating toy in the playground of quantum science and technology and we expect many exciting developments in the future.

**Acknowledgments** P.T. acknowledges fruitful discussions with D. Hunger and support by the EU project AQUOTE and the Swiss National Science Foundation. K.H. acknowledges support through the cluster of excellence QUEST at the University of Hannover. C.G. acknowledges support from the Austrian Science Fund (FWF).

## References

1. R. Hanson, D.D. Awschalom, *Nature* **453**(7198), 1043 (2008)
2. A.J. Shields, *Nat. Photonics* **1**(4), 215 (2007)
3. J. Clarke, F.K. Wilhelm, *Nature* **453**, 1031 (2008)
4. M.P. Blencowe, M.N. Wybourne, *Appl. Phys. Lett.* **77**, 3845 (2000)
5. R.G. Knobel, A.N. Cleland, *Nature* **424**, 291 (2003)
6. S. Zippilli, G. Morigi, A. Bachtold, *Phys. Rev. Lett.* **102**, 096804 (2009)
7. S.D. Bennett, L. Cockins, Y. Miyahara, P. Grütter, A.A. Clerk, *Phys. Rev. Lett.* **104**, 017203 (2010)
8. A.D. Armour, M.P. Blencowe, K.C. Schwab, *Phys. Rev. Lett.* **88**, 148301 (2002)
9. E.K. Irish, K. Schwab, *Phys. Rev. B* **68**, 155311 (2003)
10. I. Martin, A. Shnirman, L. Tian, P. Zoller, *Phys. Rev. B* **69**, 125339 (2004)
11. M.D. LaHaye, J. Suh, P.M. Echternach, K.C. Schwab, M.L. Roukes, *Nature* **459**, 960 (2009)
12. X. Zhou, A. Mizel, *Phys. Rev. Lett.* **97**, 267201 (2006)
13. E. Buks, M.P. Blencowe, *Phys. Rev. B* **74**, 174504 (2006)
14. F. Xue, Y.D. Wang, C.P. Sun, H. Okamoto, H. Yamaguchi, K. Semba, *New J. Phys.* **9**, 35 (2007)
15. Y.D. Wang, K. Semba, H. Yamaguchi, *New J. Phys.* **10**, 043015 (2008)
16. K. Jähne, K. Hammerer, M. Wallquist, *New J. Phys.* **10**, 095019 (2008)
17. S. Etaki, M. Poot, I. Mahboob, K. Onomitsu, H. Yamaguchi, H.S.J. van der Zant, *Nat. Phys.* **4**, 785 (2008)
18. I. Bargatin, M. Roukes, *Phys. Rev. Lett.* **91** (2003)
19. D. Rugar, R. Budakian, H. Mamin, B. Chui, *Nature* **430**, 329 (2004)
20. C.L. Degen, M. Poggio, H.J. Mamin, C.T. Rettner, D. Rugar, *Proc. Natl. Acad. Sci. U.S.A.* **106**, 1313 (2009)
21. F. Xue, L. Zhong, Y. Li, C.P. Sun, *Phys. Rev. B* **75**, 033407 (2007)
22. P. Rabl, P. Cappellaro, M.V.G. Dutt, L. Jiang, J. Maze, M.D. Lukin, *Phys. Rev. B* **79**, 041302 (2009)
23. M. Poggio, C. Degen, C. Rettner, H. Mamin, D. Rugar, *Appl. Phys. Lett.* **90**, 263111 (2007)
24. H. Mamin, C. Rettner, M. Sherwood, L. Gao, D. Rugar, *Appl. Phys. Lett.* **100**, 013102 (2012)
25. I. Wilson-Rae, P. Zoller, A. Imamoglu, *Phys. Rev. Lett.* **92**, 075507 (2004)
26. Yu. Makhlin, G. Schön, A. Shnirman, *Rev. Mod. Phys.* **73**, 357 (2001)
27. D. Vion, A. Aassime, A. Cottet, P. Joyez, H. Pothier, C. Urbina, D. Esteve, M.H. Devoret, *Science* **296**, 886 (2002)
28. J.A. Schreier, A.A. Houck, J. Koch, D.I. Schuster, B.R. Johnson, J.M. Chow, J.M. Gambetta, J. Majer, L. Frunzio, M.H. Devoret, S.M. Girvin, R.J. Schoelkopf, *Phys. Rev. B* **77**, 180502 (2008)
29. J.M. Raimond, M. Brune, S. Haroche, *Rev. Mod. Phys.* **73**, 565 (2001)
30. D. Leibfried, R. Blatt, C. Monroe, D. Wineland, *Rev. Mod. Phys.* **75**, 281 (2003)
31. P. Rabl, A. Shnirman, P. Zoller, *Phys. Rev. B* **70**, 205304 (2004)

32. S. Haroche, J.M. Raimond (eds.), *Exploring the Quantum* (Oxford University Press, New York, 2006)
33. A.D. O'Connell, M. Hofheinz, M. Ansmann, R.C. Bialczak, M. Lenander, E. Lucero, M. Neeley, D. Sank, H. Wang, M. Weides, J. Wenner, J.M. Martinis, A.N. Cleland, *Nature* **464**, 697 (2010)
34. M. Poggio, C.L. Degen, *Nanotechnology* **21**, 342001 (2010)
35. R. Budakian, H. Mamin, B. Chui, D. Rugar, *Science* **307**, 408 (2005)
36. D. Mozyrsky, I. Martin, D. Pelekhov, P. Hammel, *Appl. Phys. Lett.* **82**, 1278 (2003)
37. G. Berman, V. Gorshkov, D. Rugar, V. Tsifrinovich, *Phys. Rev. B* **68** (2003)
38. P. Magusin, W. Veeman, *J. Magn. Reson.* **143**, 243 (2000)
39. P. Rabl, S.J. Kolkowitz, F.H.L. Koppens, J.G.E. Harris, P. Zoller, M.D. Lukin, *Nat. Phys.* **6**, 602 (2010)
40. C.L. Degen, M. Poggio, H.J. Mamin, D. Rugar, *Phys. Rev. Lett.* **100** (2008)
41. F. Jelezko, T. Gaebel, I. Popa, A. Gruber, J. Wrachtrup, *Phys. Rev. Lett.* **92**, 076401 (2004)
42. G. Balasubramanian, P. Neumann, D. Twitchen, M. Markham, R. Kolesov, N. Mizuochi, J. Isoya, J. Achard, J. Beck, J. Tisler, V. Jacques, P. Hemmer, F. Jelezko, J. Wrachtrup, *Nat. Mater.* **8**, 383 (2009)
43. C. Degen, *Appl. Phys. Lett.* **92**, 243111 (2008)
44. J. Maze, P. Stanwix, J. Hodges, S. Hong, J. Taylor, P. Cappellaro, L. Jiang, M. Dutt, E. Togan, A. Zibrov, A. Yacoby, R. Walsworth, M. Lukin, *Nature* **455**, 644 (2008)
45. G. Balasubramanian, I. Chan, R. Kolesov, M. Al-Hmoud, J. Tisler, C. Shin, C. Kim, A. Wojcik, P. Hemmer, A. Krueger, T. Hanke, A. Leitenstorfer, R. Bratschitsch, F. Jelezko, J. Wrachtrup, *Nature* **455**, 648 (2008)
46. M. Grinolds, P. Maletinsky, S. Hong, M. Lukin, R. Walsworth, A. Yacoby, *Nat. Phys.* **7**, 687 (2011)
47. O. Arcizet, V. Jacques, A. Siria, P. Poncharal, P. Vincent, S. Seidelin, *Nat. Phys.* **7**, 879 (2011)
48. S. Kolkowitz, A.C.B. Jayich, Q. Unterreithmeier, S.D. Bennett, P. Rabl, J.G.E. Harris, M.D. Lukin, *Science* **335**, 1603 (2012)
49. S. Chu, *Nature* **416**, 206 (2002)
50. M.A. Kasevich, *Science* **298**, 1363 (2002)
51. R. Wynands, S. Weyers, *Metrologia* **42**, S64 (2005)
52. A.D. Cronin, J. Schmiedmayer, D.E. Pritchard, *Rev. Mod. Phys.* **81**, 1052 (2009)
53. W. Ketterle, D.S. Durfee, D.M. Stamper-Kurn, Bose-Einstein condensation in atomic gases, in *Proceedings of the International School of Physics "Enrico Fermi", Course CXL*, ed. by M. Inguscio, S. Stringari, C.E. Wieman (IOS Press, Amsterdam, 1999), pp. 67–176
54. I. Bloch, *Science* **319**, 1202 (2008)
55. J. Reichel, V. Vuletić (eds.), *Atom Chips* (Wiley-VCH, Weinheim, 2011)
56. D. Wineland, *Phys. Scr.* **T137**, 014007 (2009)
57. C. Deutsch, F. Ramirez-Martinez, C. Lacroûte, F. Reinhard, T. Schneider, J.N. Fuchs, F. Pichon, F. Laloë, J. Reichel, P. Rosenbusch, *Phys. Rev. Lett.* **105**, 020401 (2010)
58. D. Wineland, C. Monroe, W.M. Itano, D. Leibfried, B. King, D. Meekhof, *J. Res. Natl. Inst. Stand. Technol.* **103**, 259 (1998)
59. L. Tian, P. Zoller, *Phys. Rev. Lett.* **93**, 266403 (2004)
60. W.K. Hensinger, D.W. Utami, H.S. Goan, K. Schwab, C. Monroe, G.J. Milburn, *Phys. Rev. A* **72**, 041405(R) (2005)
61. S. Singh, M. Bhattacharya, O. Dutta, P. Meystre, *Phys. Rev. Lett.* **101**, 263603 (2008)
62. P. Treutlein, D. Hunger, S. Camerer, T.W. Hänsch, J. Reichel, *Phys. Rev. Lett.* **99**, 140403 (2007)
63. A.A. Geraci, J. Kitching, *Phys. Rev. A* **80**, 032317 (2009)
64. S. Singh, P. Meystre, *Phys. Rev. A* **81**, 041804 (2010)
65. C. Joshi, A. Hutter, F. Zimmer, M. Jonson, E. Andersson, P. Ohberg, *Phys. Rev. A* **82**, 043846 (2010)
66. S. Steinke, S. Singh, M. Tasgin, P. Meystre, K. Schwab, M. Vengalattore, *Phys. Rev. A* **84**, 023841 (2011)

67. K. Hammerer, M. Aspelmeyer, E.S. Polzik, P. Zoller, Phys. Rev. Lett. **102**, 020501 (2009)
68. K. Hammerer, K. Stannigel, C. Genes, P. Zoller, P. Treutlein, S. Camerer, D. Hunger, T.W. Hänsch, Phys. Rev. A **82**, 021803 (2010)
69. B. Vogell, K. Stannigel, P. Zoller, K. Hammerer, M.T. Rakher, M. Korppi, A. Jöckel, P. Treutlein, Phys. Rev. A **87**, 023816 (2013)
70. D. Meiser, P. Meystre, Phys. Rev. A **73**, 033417 (2006)
71. C. Genes, D. Vitali, P. Tombesi, Phys. Rev. A **77**, 050307 (2008)
72. H. Ian, Z.R. Gong, Y. Liu, C.P. Sun, F. Nori, Phys. Rev. A **78**, 013824 (2008)
73. K. Hammerer, M. Wallquist, C. Genes, M. Ludwig, F. Marquardt, P. Treutlein, P. Zoller, J. Ye, H.J. Kimble, Phys. Rev. Lett. **103**, 063005 (2009)
74. M. Wallquist, K. Hammerer, P. Zoller, C. Genes, M. Ludwig, F. Marquardt, P. Treutlein, J. Ye, H.J. Kimble, Phys. Rev. A **81**, 023816 (2010)
75. A. Bhattacharjee, Phys. Rev. A **80**, 043607 (2009)
76. C. Genes, H. Ritsch, D. Vitali, Phys. Rev. A **80**, 061803 (2009)
77. K. Zhang, W. Chen, M. Bhattacharya, P. Meystre, Phys. Rev. A **81**, 013802 (2010)
78. M. Paternostro, G. De Chiara, G. Palma, Phys. Rev. Lett. **104**, 243602 (2010)
79. G. De Chiara, M. Paternostro, G. Palma, Phys. Rev. A **83**, 052324 (2011)
80. Y. Chang, T. Shi, Y.x. Liu, C. Sun, F. Nori, Phys. Rev. A **83**, 063826 (2011)
81. Y.J. Wang, M. Eardley, S. Knappe, J. Moreland, L. Hollberg, J. Kitching, Phys. Rev. Lett. **97**, 227602 (2006)
82. D. Hunger, S. Camerer, T.W. Hänsch, D. König, J.P. Kotthaus, J. Reichel, P. Treutlein, Phys. Rev. Lett. **104**, 143002 (2010)
83. S. Camerer, M. Korppi, A. Jöckel, D. Hunger, T.W. Hänsch, P. Treutlein, Phys. Rev. Lett. **107**, 223001 (2011)
84. M. Korppi, A. Jöckel, M.T. Rakher, S. Camerer, D. Hunger, T.W. Hänsch, P. Treutlein, EPJ Web Conf. **57**, 03006 (2013)
85. D. Hunger, S. Camerer, M. Korppi, A. Jöckel, T.W. Hänsch, P. Treutlein, C. R. Phys. **12**, 871 (2011)
86. M. Gierling, P. Schneeweiss, G. Visanescu, P. Federsel, M. Häffner, D.P. Kern, T.E. Judd, A. Günther, J. Fortagh, Nat. Nanotech. **6**, 446 (2011)
87. C. Gardiner, Phys. Rev. Lett. **70**, 2269 (1993)
88. H. Carmichael, Phys. Rev. Lett. **70**, 2273 (1993)
89. C.K. Law, J.H. Eberly, Phys. Rev. Lett. **76**, 1055 (1996)
90. M. Wallquist, K. Hammerer, P. Rabl, M. Lukin, P. Zoller, Phys. Scr. **T137**, 014001 (2009)
91. T. Bagci, A. Simonsen, S. Schmid, L.G. Villanueva, E. Zeuthen, J. Appel, J.M. Taylor, A. Sorensen, K. Usami, A. Schliesser, E.S. Polzik, preprint (2013). [arXiv:1307.3467](https://arxiv.org/abs/1307.3467)
92. R.W. Andrews, R.W. Peterson, T.P. Purdy, K. Cicak, R.W. Simmonds, C.A. Regal, K.W. Lehnert, preprint (2013). [arXiv:1310.5276](https://arxiv.org/abs/1310.5276)
93. J.M. Taylor, A.S. Sørensen, C.M. Marcus, E.S. Polzik, Phys. Rev. Lett. **107**, 273601 (2011)
94. S.A. McGee, D. Meiser, C.A. Regal, K.W. Lehnert, M.J. Holland, Phys. Rev. A **87**, 053818 (2013)